Nano-Micro Letters

ISSN 2311-6706
e-ISSN 2150-5551
CN 31-2103/TB

ARTICLE

https://doi.org/10.1007/s40820-020-00484-4

Cite as
Nano-Micro Lett.
(2020) 12:145

Received: 27 April 2020
Accepted: 15 June 2020

Curtailing Carbon Usage with Addition of Functionalized $NiFe_2O_4$ Quantum Dots: Toward More Practical S Cathodes for Li–S Cells

Ning Li[1], Ting Meng[1], Lai Ma[1], Han Zhang[1], JiaJia Yao[2], Maowen Xu[1], Chang Ming Li[1] ✉, Jian Jiang[1] ✉

✉ Chang Ming Li, ecmli@swu.edu.cn; Jian Jiang, jjiang@swu.edu.cn

[1] School of Materials and Energy, and Chongqing Key Lab for Advanced Materials and Clean Energies of Technologies, Southwest University, No. 2 Tiansheng Road, BeiBei District, Chongqing 400715, People's Republic of China

[2] School of Physical Science and Technology, Southwest University, No. 2 Tiansheng Road, BeiBei District, Chongqing 400715, People's Republic of China

HIGHLIGHTS

- Using $NiFe_2O_4$ quantum dots (QDs) as additive substitutes, the total carbon content in cathodes is sharply reduced from original ~ 26% (in traditional S/C cathodes) to a low mass ratio of ~ 5%.
- The as-built S@CB ⊆ QDs demonstrate more appropriate tap density (~1.32 g cm^{-3}) and specific surface area (~19.9 m^2 g^{-1}) values than S@CB counterparts.
- $NiFe_2O_4$ QDs additives possess superb chemisorption interactions with Li_2Sn molecules and proper charge-transfer/catalytic features to strengthen redox kinetics of overall cathode systems.

ABSTRACT Smart combination of manifold carbonaceous materials with admirable functionalities (*like* full of pores/functional groups, high specific surface area) is still a mainstream/preferential way to address knotty issues of polysulfides dissolution/shuttling and poor electrical conductivity for S-based cathodes. However, extensive use of conductive carbon fillers in cell designs/technology would induce electrolytic overconsumption and thereby shelve high-energy-density promise of Li–S cells. To cut down carbon usage, we propose the incorporation of multi-functionalized $NiFe_2O_4$ quantum dots (QDs) as affordable additive substitutes. The total carbon content can be greatly curtailed from 26% (in traditional S/C cathodes) to a low/commercial mass ratio (~ 5%). Particularly, note that $NiFe_2O_4$ QDs additives own superb chemisorption interactions with soluble Li_2S_n molecules and proper catalytic features facilitating polysulfide phase conversions and can also strengthen charge-transfer capability/redox kinetics of overall cathode systems. Benefiting from these intrinsic properties, such hybrid

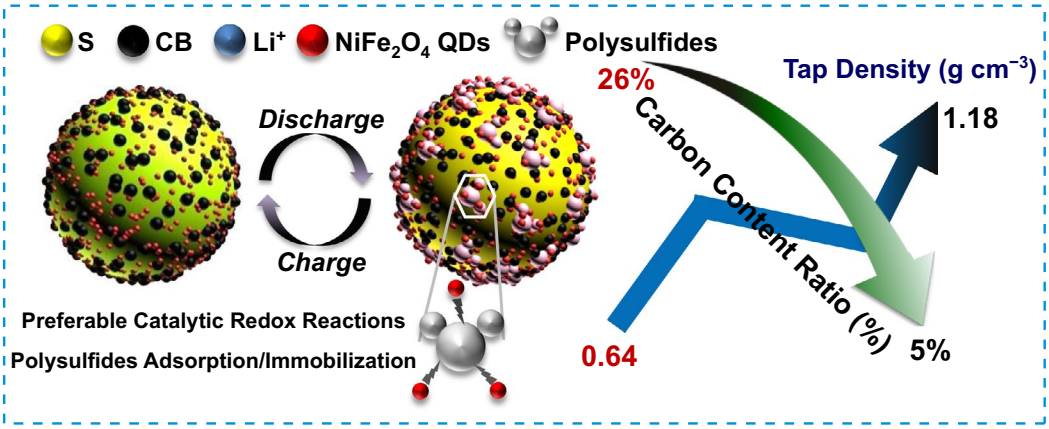

Published online: 11 July 2020

cathodes demonstrate prominent rate behaviors (decent capacity retention with ~ 526 mAh g^{-1} even at 5 A g^{-1}) and stable cyclic performance in $LiNO_3$-free electrolytes (only ~ 0.08% capacity decay per cycle in 500 cycles at 0.2 A g^{-1}). This work may arouse tremendous research interest in seeking other alternative QDs and offer an economical/more applicable methodology to construct low-carbon-content electrodes for practical usage.

KEYWORDS Carbon usage reduction; $NiFe_2O_4$ quantum dots; Additive substitute; Practical S cathode; Li–S cells

1 Introduction

Increasing demands for emerging electric vehicles and surplus electricity storage have trigger searches for next-generation energy-storage systems. Nowadays, Li–S cells are extremely admirable and encouraging given their great theoretical gravimetric/volumetric capacities, good environmental benignity, and pretty low cost due to abundant natural reserves of S [1–3]. Unfortunately, their practical applications are put off by three major constraints including: (i) inferior conductivity of either S/Li_2S cathodes or their intermediate/end-discharge products (causing sluggish redox reaction kinetics and less actives utilization ratio), (ii) huge volume expansions (e.g., ≈ 80% for S cathode) and notorious Li dendrite formation (undermining their long-term electrochemical stability/cyclic lifespan), and (iii) intractable polysulfide dissolution in organic electrolytes (inducing irreversible capacity decay and unstable Coulombic efficiency) [4, 5]. Aimed at tackling the above challenges, one prioritized strategy is the combination of functionalized carbonaceous frameworks (made up of hierarchically porous graphene, biomass-derived microporous carbon, or metallic organics [6–8]) with S or Li_2S to offset the electrode conductivity and operation stability [9, 10]. However, once the amount of such carbon fillers reaches a critical value of 50 wt% in cathodes, there would give rise to many troublesome issues for real applications [11]. Primarily, overusing carbons with large specific surface areas (100–1500 $m^2\ g^{-1}$) and low tap density (0.1–0.3 g cm^{-3}) results in a sponge-*like* cathode that requires flooded electrolyte to sufficiently wet all electrode regions. This predicatively intensifies the electrolyte-to-sulfur (E/S) ratio and battery weight, thereby diminishing the total cell specific energies [12]. Additionally, carbons' hydrophobicity is adverse to organic electrolyte wettability, resisting Li^+ transport at the solid–liquid interface and deteriorating the cell kinetics. Standing on internal chemical interactions, nonpolar carbon species are incompetent to work with polar polysulfides for long cyclic stability and capacity retention [13]. For commercial concerns of Li–S cells, scientists require to introspect shortcomings in current cell technology and devote to seeking for other feasible/rational solutions.

The use of functionalized quantum dots (QDs) with a typical sub-30 nm size (comparable to that of carbon black conducting agent) may be a better option due to their great volume-to-surface ratio, far less invalid pore volumes, high specific surface energy, and enriched dangling bonds beneficial for chemical adsorption. For example, Xu et al. once employed a very small amount of black phosphorus QDs as electrocatalysts, which can adsorb soluble polysulfide intermediates and meantime promote their conversions into solid-state Li sulfides due to numerous catalytic anchors on QDs edges. The integrated hybrid cathodes showcase rapid reaction kinetics without evident shuttling effects, showing a slow capacity decay rate (~ 0.027% per cycle) among all 10^3 cycles [2]. Park et al. reported the addition of graphene QDs into S cathodes can induce the formation of hierarchically functionalized S/carbon hybrids aided by involved O-rich groups on QDs. The robust C-S bonding can minimize irreversible losses of polysulfide anions, enabling good capacity retention (~ 1000 mAh g^{-1} after 100 cycles at 0.5 C) and fast charge-transfer behaviors (remarkable discharge capacity of ~ 540.17 mAh g^{-1} at 10 C) [14]. Hence, alternatively utilizing QDs would be highly useful for Li–S cells operation, which holds great promise in reducing carbon usage amount, thus lowering the electrolyte consumption and ensuring gravimetric/volumetric specific energies of devices.

Some transitional metal oxides have been paid special attention as both physicochemical adsorbers for Li polysulfide intermediates and good catalysts to boost long-chain Li_2S_n ($n = 3–8$) conversion into insoluble species and meantime accelerate substance transitions forward solid-date Li_2S/Li_2S_2 [15, 16]. Ferruginous oxide families (e.g., FeO, Fe_2O_3, Fe_3O_4), the most economical and welcome material candidates, own favorable chemical bonding to polysulfide molecules and obey reversible adsorption/

 https://doi.org/10.1007/s40820-020-00484-4

desorption mechanism based on strong polar surface or *Lewis* acid—base interactions [17–19]. Another recognized prototype material should be designated to Ni-based oxides (e.g., Ni_2O_3, NiO, β-NiOOH), which can speed up redox reaction kinetics aided by their superb electrocatalytic activities deriving from their surface/sub-surface defects or vacancies [20–22]. As a mixed combination of Fe and Ni oxides, $NiFe_2O_4$ might be a better choice than aforementioned since it would not only anchor dissociative polysulfide species and suppress the adverse "shuttling effect" during charge/discharge procedures, but also promote cell kinetics thanks to its positive catalytic properties (e.g., expediting sulfide redox couples S^{2-}/S_n^{2-} conversion) [23]. The extra incorporation of semi-conducting $NiFe_2O_4$ (conductivity: 74.32 S cm^{-1}) into cathode systems would further reinforce the electrons-transfer capability of entire electrode systems.

We herein attempt to minimize the total carbon usage by alternative use/addition of multi-functionalized $NiFe_2O_4$ QDs with a characteristic fluorescence effect at 568 nm (excitation wavelength: 325 nm, see Fig. S1) into cathode systems, aiming at building more efficient and practical Li–S cells. The implanted $NiFe_2O_4$ QDs are able to serve as "modular building blocks" in optimized electrodes for Li_2S_n localization/catalysis because of their good electrical conductivity and ample anchoring sites on external surface. The as-configured cathodes would not only own a proper ability of inherent chemisorption/interactions with polysulfides but also fast charge-transfer and redox reaction kinetics. Particularly, note that by choosing $NiFe_2O_4$ QDs as additive substitutes, the overall carbon content in cathodes is reduced to a minimal level of 5%, avoiding the excessive electrolyte consumption and guaranteeing specific energy parameters. To affirm such functionalities of $NiFe_2O_4$ QDs, we have deliberately evaluated cell performances in electrolyte solutions without extra addition of $LiNO_3$. As confirmed, QDs-involved cathodes showcase a great specific capacity of 921.1 mAh g^{-1} at 0.2 A g^{-1}, decent rate capability (remaining 526 mAh g^{-1} at 5 A g^{-1}), and very impressive cyclic stability over 500 cycles (capacity decay rate: 0.08% per cycle at 0.2 A g^{-1}; almost all Coulombic efficiencies beyond 96%). The concept of "building cathodes of Li–S cells with cost-effective, durable and versatile QDs" may arouse global research interest in designing well-fitted/compatible mixed metal oxide species and construction of low-carbon-content electrode for more practical Li–S cells.

2 Experimental Section

2.1 Preparation of $NiFe_2O_4$ QDs

Typically, ~ 1.62 g ferric chloride (purity > 99.99%, *Sigma-Aldrich*) and ~ 1.45 g nickel chloride (purity > 99.99%, *Alfa*) are dissolved into ~ 80 mL of deionized water with an ultrasonication treatment for 30 min. The resultant solution is magnetically stirred at ambient atmospheres and dripped with concentrated ammonia (*Sigma-Aldrich*) until the solution pH value reaches 8. After vigorously stirring for 10 min, the obtained mixture is transferred into a Teflon-lined stainless-steel autoclave and heated at 190 °C for 10 h. When cooled down to room temperature naturally, red powder samples are fetched out by centrifugation, washed with deionized water and ethanol several times, and dried at 60 °C for later use.

2.2 Preparation of S@CB⊆QDs Cathodes

S@CB⊆QDs hybrid samples are obtained by a heat treatment toward uniform powder mixtures containing ~ 8.5 g of sublimed S (*Sigma-Aldrich*), ~ 0.5 g carbon black (CB; *Ketjenblack EC-300 J*), and ~ 1 g of as-made $NiFe_2O_4$ QDs at 165 °C for 12 h. For cathode fabrication, such hybrid powders are carefully grinded, mixed with PVDF (*Sigma-Aldrich*) at a mass ratio of 9:1, and dispersed into moderate NMP (*Fluka*, 40 mg mL^{-1}) to form homogeneous slurry. The calculated S ratio for S@CB⊆QDs cathodes is 76.5% in theory (if excluding the polymer binder mass, the theoretical S ratio should be ~ 85%). The slurry is then pasted onto an aluminum foil and dried at 60 °C for 10 h in a vacuum oven. For comparison study, the counterpart of S@CB hybrids is also prepared using the same procedures without the addition of $NiFe_2O_4$ QDs.

2.3 Materials Characterization and Electrochemical Testing

Fluorescent properties for QDs are measured by using a fluorescence spectrophotometer (FluoroMax-4, HORIBA, Japan). Phase structures of specimens are characterized by X-ray powder diffraction (XRD; D8 Advanced diffractometer with Cu Kα radiation, λ = 1.5418Å). The subtle geometric morphology and crystalline structure are detected

by field emission scanning electron microscopy (FESEM, JEOL JSM-6700F) and transmission electron microscopy (HRTEM, JEM-2010F) equipped with energy-dispersive X-ray spectroscopy (EDS). In order to clarify the surface compositions, X-ray photoelectron spectroscopy (XPS; PerkinElmer model PHI 5600 spectrometer) is employed as well. The Raman spectra are recorded on a Renishaw 1000 NR Ar laser Raman spectroscope (532 nm laser) at ambient atmospheres. Thermogravimetric (TG; SDT600, USA) is also performed to determine the mass content under N_2 atmospheres. Tap density values for synthesized samples (S@CB ⊆ QDs, S@CB, $NiFe_2O_4$ QDs) are determined by a tapping tester (JF-20, Xiamen, China; vibration frequency: 250 tap min^{-1}; amplitude: 3 mm; total counter: 8000 times). Other tap density parameters for commercial CB (0.25 mg cm^{-2}) and sublimed S powders (1.2 mg cm^{-2}) are directly obtained from reagent suppliers. All 2032-type coin cells are assembled with a cathode (S@CB ⊆ QDs or S@CB), a Li foil anode, and a separator (Celgard 2300 membrane, purchased from *Sigma-Aldrich*) in an Ar-filled glovebox (Mikrouna Super; $H_2O < 0.1$ ppm, $O_2 < 0.1$ ppm). The electrolyte for Li–S cell testing is 1 M lithium bis-(trifluoromethanesulfonyl) imide dissolved in 1,3-dioxolane and dimethoxymethane (1:1 by volume) solvent. To clarify the actual S loading of tested electrodes (size: 12 mm), we have purposely measured the involved S content toward electrode specimens in the same batch. The actual S mass loading is eventually determined to be ~ 4.7 ± 0.1 mg per cell by a thermal treatment. The electrolyte/sulfur (E/S) ratio herein is measured to be a central value of ~ 4.26 μL mg^{-1}. On a CS310 electrochemical workstation, the cyclic voltammetry (CV) test is conducted between ~ 1.6 and ~ 2.8 V at a scan rate of ~ 0.1 mV s^{-1}, and the electrochemical impedance spectroscopy (EIS) measurements are carried out from 100 kHz to 0.1 Hz. Galvanostatic charge/discharge tests are conducted at varied current densities within a cutoff voltage window of 1.6–2.8 V using a professional battery tester (Land, China). To check the polysulfide adsorption ability, ~ 50 mg $NiFe_2O_4$ QDs are added into 5 mL ~ 0.3 mol L^{-1} Li_2S_6 solution (pre-made by dissolving Li_2S and S with a molar ratio of 1:5 into dimethoxymethane under vigorously stirring at 80 °C).

3 Results and Discussions

3.1 Basic Morphological and Structural Characterization

The schematic illustration in Fig. 1 manifests the general working mechanism of $NiFe_2O_4$ QDs in cathodes for Li–S cells. Generally, current mainstream materials combined with S or Li_2S actives are still various bulky frameworks/matrix made up of hierarchically porous graphene, biomass-derived microporous carbons or high-specific-surface metallic organics. However, these S reservoir scaffolds are proven imperfect for actives loading due to (i) overmuch presence of spatial void places that are doomed to need flooded/excess electrolyte solution for complete electrode infiltration and (ii) lack of strong/polar binding interactions for anchoring dissociative molecules. In contrast, the ternary material $NiFe_2O_4$ itself has pronounced chemisorption/catalytic activities for soluble Li_2S_n intermediates, and meanwhile good electrical conductivity to compensate undesired intrinsically insulating properties of S-based actives. Moreover, its QDs form enables good organic electrolyte wettability and more exposed active spots on surface for polysulfide immobilization. In a crystalline structure of $NiFe_2O_4$ QDs, both Ni and Fe atoms can provide large quantities of chemisorption sites on surface edges to confine Li_2S_n molecules via electrostatic interactions, and meanwhile Ni constituents would improve Li_2S nucleation rate through strong-binding vacancy sites and catalytically accelerate their phase conversion. In particular, the smart use of $NiFe_2O_4$ QDs substitutes entails a fact that all involved carbon content in cathodes can be largely decreased to an extremely low level of 5%, thus forming more dense/compact electrodes rather than ones full of internal pores [24]. Practically, it is surprising to notice these functional $NiFe_2O_4$ QDs can evenly integrate with S@CB to form highly dispersive and individual units; thereby, S actives together with their derivatives yielded in charge/discharge processes would be firmly restricted nearby QDs or local positions inside cathode regions. Besides, aided by efficient electrochemical catalysis of $NiFe_2O_4$ QDs, the assembled Li–S cells can exhibit very stable cyclic behaviors even without the extra addition of $LiNO_3$ into the electrolyte solution, as discussed in later sections [25, 26].

https://doi.org/10.1007/s40820-020-00484-4

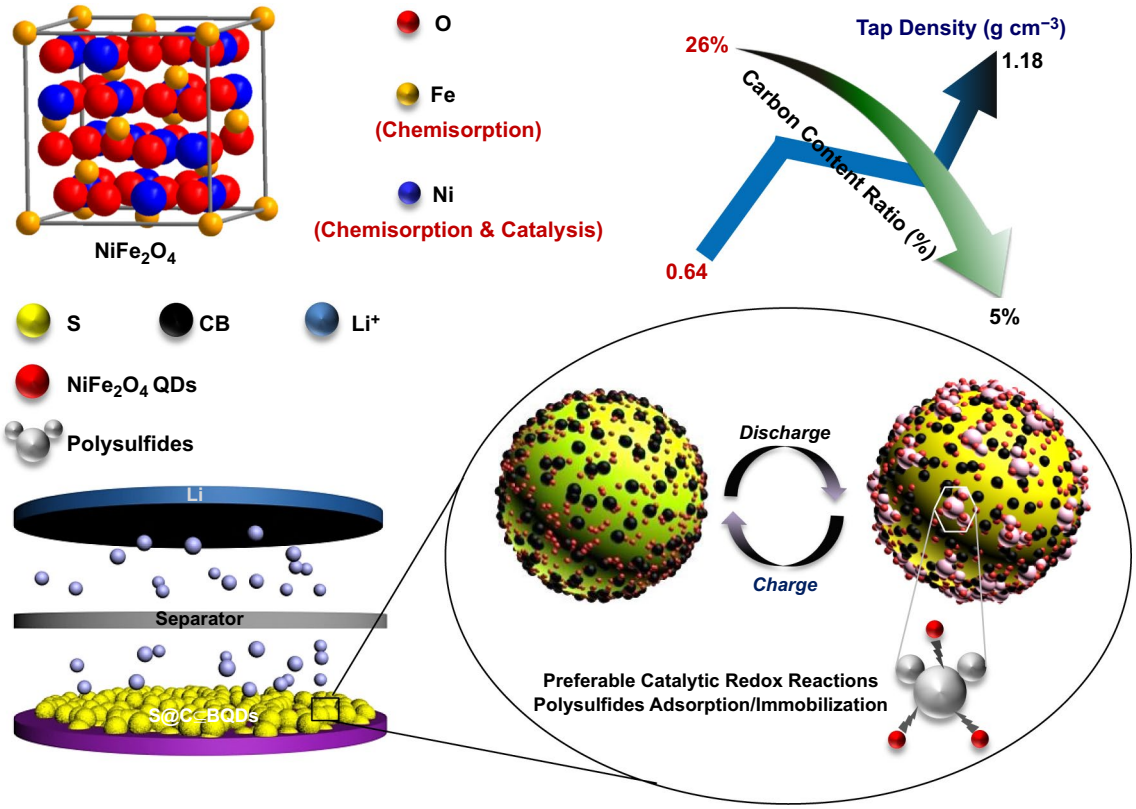

Fig. 1 General schematics showing configured devices of (−)Li//S@CB⊆QDs(+) and the working mechanism of $NiFe_2O_4$ QDs

Then, the structural information of $NiFe_2O_4$ QDs has been examined by FESEM and TEM (Fig. 2a–c). Basic top-view FESEM and TEM observations reveal fresh $NiFe_2O_4$ QDs are evenly dispersed in the absence of any aggregations. The statistical analysis on QDs (Fig. 2d) reflects that their mean diameter size is centralized at ~ 7.88 nm within a standard deviation of ~ 1.66 nm. The well-defined crystalline lattices with spacing distances of ~ 0.25 and ~ 0.29 nm successively correspond to the characteristic (311) and (220) lattice planes of cubic $NiFe_2O_4$ (JCPDS No. 74-2081). Figure 2e, f shows typical FESEM and EDS detections on ultimate S@CB⊆QDs samples to uncover their delicate geometric/inherent properties. We note that such foreign $NiFe_2O_4$ QDs have perfectly coalesced with S@CB nanoparticles to form individual hybrid nano units (average size: ~ 150 nm) instead of micro bulks. The EDS spectrum (inset in Fig. 2f) and mapping results (Fig. 2g–l) further affirm the homogenous elemental distribution of Ni, Fe, O, S, and C in specimens. Their TEM observations (Fig. S2a, b) clearly reveal that there evenly distribute plenty of $NiFe_2O_4$ QDs (size: ~ 10 nm) and CB nanoparticles (size: ~ 30 nm) surrounding the S matrix, confirming the successful hybrid construction of S@CB⊆QDs products (though close HRTEM observations toward interfaces between $NiFe_2O_4$ QDs and S are hardly achieved due to evident S sublimation under the high-energy electron beam condition, we successfully capture the significant information on robust $NiFe_2O_4$ QDs/CB interfaces and prominent adhesive capabilities for $NiFe_2O_4$ QDs; see Fig. S2c). The XRD pattern (Fig. S3) depicts the samples' crystallographic phase at distinct evolution stages. Obviously, diffraction peaks detected at 28.4°, 34.8°, 42.5°, 53°, and 62.3° in both $NiFe_2O_4$ QDs and S@CB⊆QDs samples correspond well to (220), (311), (400), (422), (511), and (440) facets of cubic $NiFe_2O_4$ (JCPDS card No. 74-2081; space group: Fd-3 m). After S infusion, intense peaks emerging at 21.1°, 22.3°, 25°, 25.9°, 27°, 27.9°, and 30.6° can be all indexed to monoclinic S (JCPDS card No. 74-2107; space group: P-21). The Raman peaks at ~ 143, ~ 202, ~ 289, ~ 548, and ~ 665 cm^{-1} (Fig. S4) successively correspond to T_{2g} (1), E_g, T_{2g} (3) and A_{1g} modes for cubic $NiFe_2O_4$, keeping in line with previous literature [27–29]. Peak signals at ~ 143 and ~ 202 cm^{-1} (T_{2g} (1) mode)

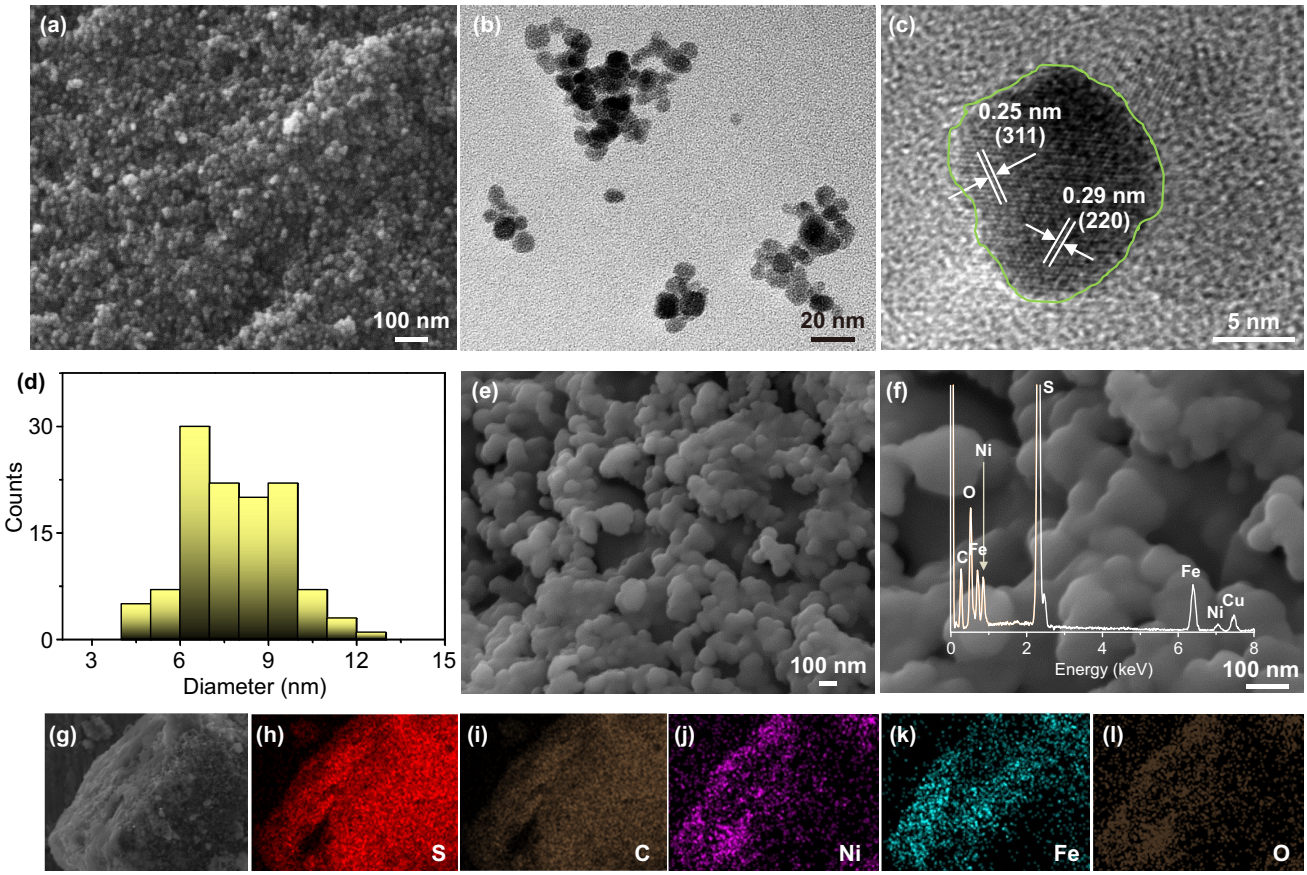

Fig. 2 **a** Basic SEM, **b**, **c** TEM observations, and **d** size-distribution plot of $NiFe_2O_4$ QDs. **e**, **f** SEM images (inset: EDS spectrum) and **g**–**j** elemental mappings of S@CB⊆QDs

are mainly assigned to Fe–O vibrations due to the translational movement of tetrahedron atoms, while the ones at ~ 289 cm^{-1} (E_g mode) and ~ 548 cm^{-1} (T_{2g} (3) mode) result from symmetric bending of O with respect to Fe/Ni atoms and vibrations of octahedral groups. The symmetric stretching of Fe–O or Ni–O bonds in $NiFe_2O_4$ would also lead to a *Raman* peak at ~ 665 cm^{-1} (A_{1g} mode). The additional visible peak at a wavenumber of ~ 464 cm^{-1} comes from the elemental S, and other two strong peaks at ~ 1346 and ~ 1585 cm^{-1} are ascribed to fingerprint D and G bands for CB, respectively. Besides, the TG measurement (Fig. S5) declares the total S weight percentage is up to ~ 75 wt% in S@CB⊆QDs.

The physical density of commercial CB, sublimed S, S@CB⊆QDs, and pure $NiFe_2O_4$ QDs is visually compared, as presented by a photograph in Fig. 3a. All sample powders are pre-tapped for efficient materials packing. Also, their key parameters of tap density and specific surface areas are successively plotted in Fig. 3b, c. The tap density value of CB is as low as ~ 0.25 g cm^{-3}, over four times less than S (~ 1.26 g cm^{-3}) and $NiFe_2O_4$ QDs (~ 1.43 g cm^{-3}). By contrast, the specific surface area of CB even reaches a value of ~ 800 cm^2 g^{-1} (the standard is given by CB suppliers), far higher than that of either $NiFe_2O_4$ QDs (~ 80.8 cm^2 g^{-1}) or S (~ 9.3 cm^2 g^{-1}). Consequently, excessive use of sparse carbons is doomed to consume overmuch electrolytes to infiltrate all interior surfaces in cathodes, augmenting cells weight and lowering their specific energy. To make dense cathodes with minimized electrolyte uptake, practical S hosts are ought to own proper surface areas (< 100 m^2 g^{-1}) and tap density (0.7–1 g cm^{-3}), as declared in recent literature [11]. By employing $NiFe_2O_4$ QDs as additive substitutes, the as-formed S@CB⊆QDs possess more appropriate tap density (~ 1.32 g cm^{-3}) and specific surface area (~ 19.9 m^2 g^{-1}) values than S@CB counterparts, holing great potential in Li–S cell applications.

https://doi.org/10.1007/s40820-020-00484-4

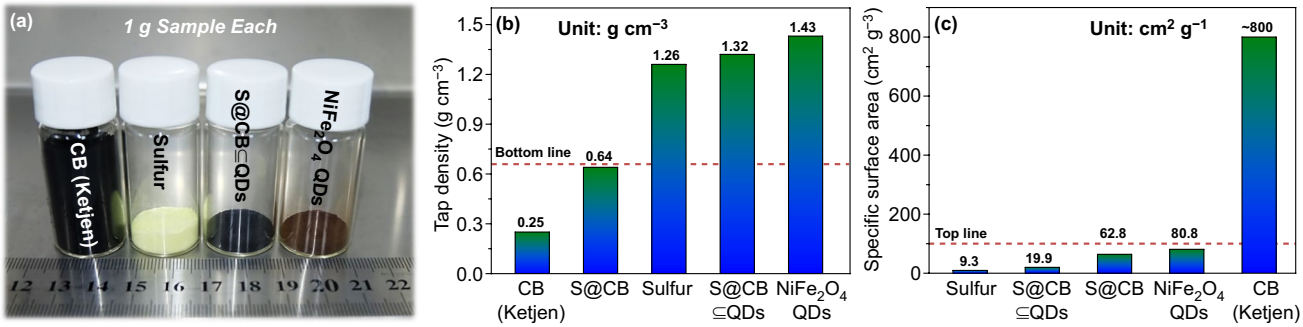

Fig. 3 **a** A visual photograph of 1 g pre-tapped CB, S, S@CB⊆QDs and $NiFe_2O_4$ QDs powder samples. Parameter comparisons on the **b** tap density and **c** specific surface area of CB, S, S@CB, S@CB⊆QDs, and $NiFe_2O_4$ QDs

3.2 Electrochemical Testing and Analysis

The catalytic effects of $NiFe_2O_4$ QDs for polysulfide conversion kinetics are primarily probed by cyclic voltammetry (CV) method in a voltage window of −0.5 to 0.5 V for Li_2S_6 symmetric cells. To exclude irrelevant influences, we also intentionally plot the CV curve of S@CB for a clear comparison study (Fig. 4a). S@CB⊆QDs electrodes exhibit far higher CV response than S@CB, confirming their superior electrochemically catalytic behaviors [30, 31]. This should be associated with a unique phenomenon that electropositive Fe atoms at corner sites (Fig. 1) tend to leach out by polysulfide etching, leaving rich vacant defects around Ni sites and hence facilitating/activating redox reactions [32]. An visualized adsorption experiment is further performed by adding $NiFe_2O_4$ QDs into a Li_2S_6 solution (~0.3 mol L^{-1}) to testify their absorption ability (Fig. 5b). Compared to pure concentrated Li_2S_6 solution, $NiFe_2O_4$ QDs-contained liquid becomes colorless after few hours, solidly certifying the excellent chemisorption capability of QDs toward Li_2S_n. To better confirm practical functions of $NiFe_2O_4$ QDs in full-cell operation, we have purposely excluded positive effects/contributions (e.g., on Li_2S_n shuttling suppression) from additive salts and executed all cell measurements in $LiNO_3$-free electrolytes. Figure 4c shows CV curves of S@CB⊆QDs cathodes between 1.6 and 2.8 V (*vs.* Li/Li^+) at a scanning rate of 0.1 mV s^{-1} for initial five cycles. Cathodic peaks at ~2.38 and ~2.1 V are ascribed to the electrochemical transformation of S_8 into long-chain polysulfide species and further reductions into solid Li_2S_2/Li_2S, respectively. In subsequent anodic scans, the overlapped anodic peaks at ~2.58 V result from reverse complex oxidation reactions from Li_2S_n ($n = 1 - 2/4 - 8$) to pristine S_8 [33–35]. With regard to S@CB cathodes (Fig. S6), there are similar cathodic/anodic peaks but obvious potential polarization/sluggish phenomena accompanied in early cyclic periods. The onset potential positions for characteristic redox peaks of S@CB⊆QDs and S@CB are also labeled, respectively (see CV plots in Fig. S6). The anodic peak of S@CB⊆QDs is initiated at ~2.39 V, whereas the two-step cathodic peaks are successively lying at ~2.51 V (corresponding to S_8 transformation into long-chain Li_2S_n ($n \geq 4$)) and ~2.17 V (indexed to changes from low-order Li_2S_n ($n < 4$) to Li_2S). Compared to S@CB cases with a higher anodic peak position of ~2.43 V and lower cathodic ones at ~2.46 and ~2.16 V, $NiFe_2O_4$ QDs-involved electrodes demonstrate upper electrochemical activities and lowered energy barriers for the onset of redox peaks. Such enhanced redox reaction kinetics are closely associated with intrinsic positive effects deriving from $NiFe_2O_4$ QDs, which can electrocatalytically push forward electrochemical conversions of S-based active species.

Galvanostatic charge–discharge curves of S@CB⊆QDs under 0.1 A g^{-1} at the 1st, 50th, 100th, 300th, and 500th cycle (Fig. S7) reveal two distinct plateaus appear at ~2.38 and ~2.1 V, which are in accordance to classic multi-step reductions of S_8. The presence of a long and flat plateau at ~2.58 V agrees well with our former CV analysis. Even after 500 times of deep cycling, the well-defined presence of such characteristic voltage plateaus affirms the durable redox kinetics and cyclic performance of S@CB⊆QDs. Figure 4d shows the long cyclic records of S@CB and S@CB⊆QDs at 0.2 A g^{-1}. S@CB⊆QDs hybrids can deliver a remarkable discharge capacity of ~910 mAh g^{-1} and inappreciable

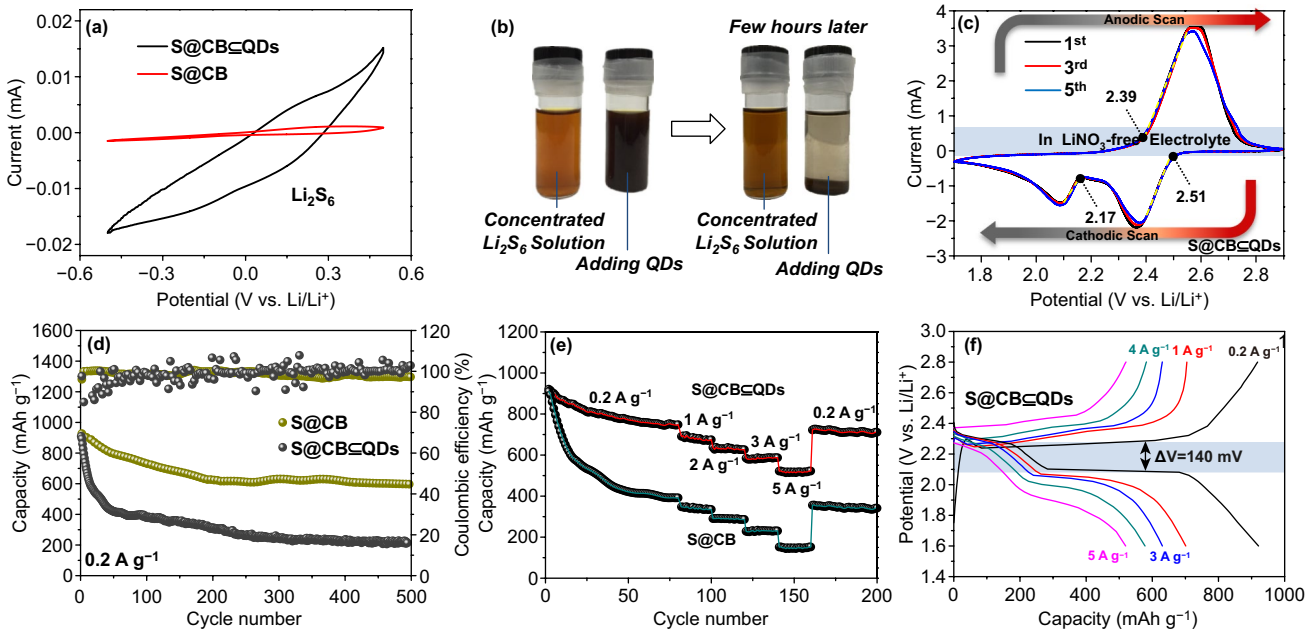

Fig. 4 **a** CV curve comparisons between QDs-involved and QDs-free cathodes. **b** Adsorption ability of $NiFe_2O_4$ QDs in Li_2S_6 electrolyte. Electrochemical testing results on S@CB⊆QDs: **c** CV curves, **d** long-term cyclic performance, **e** rate-varied cyclic record and **f** rate-varied voltage profiles

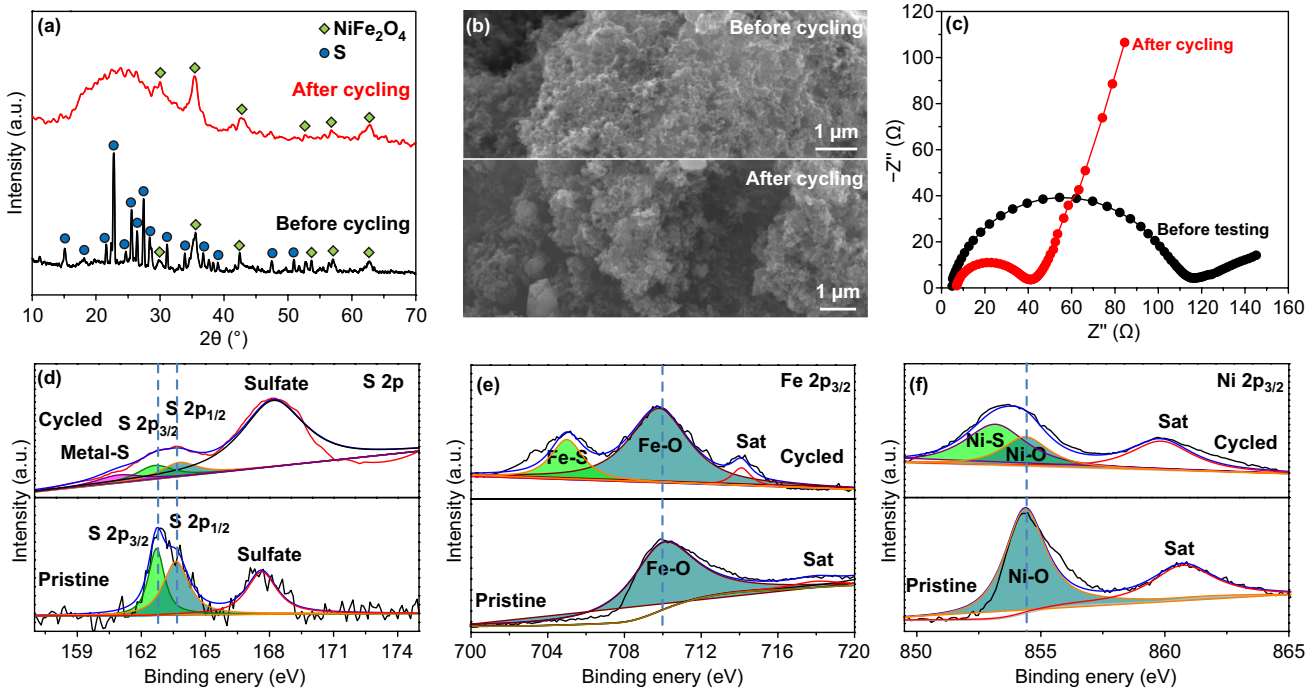

Fig. 5 Comparison analysis of S@CB⊆QDs before and after 500 cycles via techniques of **a** XRD, **b** SEM, **c** EIS and **d-f** XPS: **d** S 2p, **e** Fe $2p_{3/2}$, and **f** Ni $2p_{3/2}$

https://doi.org/10.1007/s40820-020-00484-4

capacity fading (only ~ 0.09% per cycle) even after 500 cycles with all Columbic efficiencies over 96%. In sharp contrast, after limited 100 cycles, S@CB cathodes exhibit only ~ 43.8% of initial capacity (~ 908 mAh g^{-1}), along with very fluctuant/unsteady Columbic efficiency records (values jumping between 82% and 109%). Given the cathode diameter is 12 mm (electrode area: ~ 1.13 cm^2), the areal capacity value for S@CB ⊆ QDs cathodes is measured as high as ~ 3.83 mAh cm^{-2}. When compared to S@CB and other metal oxide-based cathode examples (please see the added plot in Fig. S8), the areal capacity of S@CB ⊆ QDs is much higher than the value of S@CB, or even double/triple times that of counterparts (e.g., S/Co_3O_4/C, S/NiO/C, TiO_2 QDs@MXene/S) [1–4].

Figure S9 shows the EIS testing results fitted by the inset *Randles* equivalent circuit. R_1 in the circuit model represents the bulky resistance caused by the electrolyte phase as well as other parts of cell configurations, corresponding to the intercept with the real axis at a high-frequency range. There is no large difference in R_1 between these two electrodes; the R_1 value (~ 1.58 Ω) of S@CB is a bit lower than that of S@CB ⊆ QDs (~ 4.89 Ω), which may be induced by the increment of local electrolyte absorption/concentration for carbon-rich cathodes. R_2 and CPE_1 successively represent the charge-transfer resistance and related capacitance reflecting the kinetic nature at the solid/electrolyte interface. S@CB ⊆ QDs electrodes own a smaller R_2 value (~ 114.8 Ω) than S@CB counterparts (~ 159.7 Ω), suggesting their upper physicochemical properties aided by the addition of $NiFe_2O_4$ QDs. W_1 refers to the diffusion impedance correlating with Li^+ diffusion processes through a bulk cathode, as reflected by a tail-*like* slope at the low-frequency range [25, 36]. A larger slope of S@CB ⊆ QDs electrode indicates their superior mass-transfer behaviors for Li^+. The corresponding Li^+ diffusion coefficient (D_{Li}) and double layer capacitance (C_d) can be calculated according to formulas below:

$$D_{Li} = \frac{R^2T^2}{2A^2n^4F^4c^4\sigma^2} \quad (1)$$

$$C_d = \frac{1}{R_{ct}} \quad (2)$$

where R refers to the gas constant (8.3143 J K^{-1} mol^{-1}), T is the absolute temperature, A is the area of electrode, n is the number of electrons involved in the reaction, F is the *Faraday* constant, C_{Li} is the Li^+ concentration, σ is the *Warburg* factor, and ω is the angular velocity. Figure S10 reflects the S@CB ⊆ QDs cathode even possesses a higher D_{Li} (4.14×10^{-8} cm^{-2} s^{-1}) than S@CB (0.52×10^{-8} cm^{-2} s^{-1}), which is possibly associated with shortened Li^+ diffusion paths or surface ion diffusivity due to less carbon usage [37]. Moreover, the C_d of S@CB ⊆ QDs cathode (7.3×10^{-7} F) is far lower than that of S@CB (1.74×10^{-6} F), mainly attributing to diminished specific areas of S@CB ⊆ QDs. The rate performance (Fig. 4e) is also estimated at different current rates from 0.2 to 5 A g^{-1}. Apparently, the average discharge capacity of S@CB ⊆ QDs electrodes slightly drops from 910 to 691, 636, 589, and 526 mAh g^{-1} when the current rate stepwise increases from 0.2 to 1, 2, 3, and 5 A g^{-1}, whose records are much better than those of S@CB (901, 352, 287, 226, and 153 mAh g^{-1}). Figure 4f displays typical voltage profiles of S@CB ⊆ QDs. Specifically, S@CB ⊆ QDs cathodes exhibit relatively lower potential polarization ($\Delta V = 140$ mV) when compared to S@CB cases ($\Delta V = 365$ mV; Fig. S11), declaring effectively improved cell kinetics due to the addition of $NiFe_2O_4$ QDs. To further make clear effects induced by S loading ratio, basic electrochemical behaviors of cathodes with ramped S areal mass densities (including 4, 8, 10, and 12 mg cm^{-2}) have been provided for comparative study (Fig. S12). Similar to the former case (~ 754 mAh g^{-1}) under an areal mass of ~ 4 mg cm^{-2}, S@CB ⊆ QDs cathodes (at ~ 8 mg cm^{-2}) can maintain a comparable reversible capacity of ~ 702 mAh g^{-1}. However, when S loading rises to a level of 10 or 12 mg cm^{-2}, the evident capacity degradations of S@CB ⊆ QDs cathodes are noticed (Fig. S12a), with delivered specific capacities of ~ 465 and ~ 266 mAh g^{-1}, respectively. (Corresponding specific capacity vs. mass loading plot is displayed in Fig. S12b.) This is mainly attributed to a fact that such a highly thicken/compact electrode film is not beneficial for electrolytic infiltration, leading to reduced actives utilization and deteriorated electrode operation stability (see Coulombic efficiency record in Fig. S12c; especially when S areal mass increases to 12 mg cm^{-2}, huge fluctuations on Coulombic efficiency values are rather distinct).

3.3 Postmortem Analysis on Cycled Cathodes

Postmortem analysis on cycled cathodes is systematically conducted as well. Figure 5a shows the XRD pattern of S@CB ⊆ QDs after 500 cycles. All detectable diffraction peaks accord well with those belonging to $NiFe_2O_4$ QDs, except for a broad bump-like diffraction peak at ~ 23.3° stemming from electrolytic residuals; no other possible substances (e.g., FeS, FeO_x, NiS, and NiO) are probed,

confirming the outstanding electrochemical stability of $NiFe_2O_4$ QDs. The geometrical morphology of fatigue S@CB⊆QDs cathodes (Fig. 5b) clearly reveals the absence of any flower-like S crystals formation. Elemental mapping records (Fig. S13) further evidence the same uniform distribution of Ni, Fe, O element as before. The EIS testing toward S@CB⊆QDs cathodes before and after 500 cycles have been compared (Fig. 5c). The R_2 for cycled S@CB⊆QDs electrodes (~40.3 Ω) is far lower than the value of fresh ones (~114.4 Ω), which might be due to remarkable reconfiguration/rearrangement of S actives in cathode regions among repeated charge/discharge processes. A higher slope suggests Li^+ transfer rate is also enhanced due to the setup of electrochemical reaction equilibrium preferable for redox conversion. Their surface chemistry and composition are further analyzed by XPS (Fig. 5d–f). The pristine S 2p spectrum exhibits a typical spin–orbit doublet at ~162.7 (S $2p_{3/2}$) and ~164.1 eV (S $2p_{1/2}$), successively attributing to the terminal and bridging S (Fig. 5d) [38]. The additional peak situated at ~167.6 eV refers to sulfate species resulted from oxidation during sample synthesis. In contrast, great changes in S 2p spectrum have been observed for cycled electrodes owing to the presence of intensified peak centralized at ~167.3 eV, which is mostly responsible for the formation of metal (Fe or Ni)-S bonds via dangling bonds on $NiFe_2O_4$ QDs [39]. Inherent interaction protocols aforementioned are also validated by Fe $2p_{3/2}$ and Ni $2p_{3/2}$ spectra. Figure 5d compares the Fe $2p_{3/2}$ spectrum of S@CB⊆QDs cathode before and after cycling. The initial Fe $2p_{3/2}$ core-level spectrum (Fig. 5e) exhibits a characteristic peak (~710.4 eV) as well as one shake-up satellite peak (~719.1 eV), indicative of a typical Fe^{3+} (Fe–O bond) chemical state. After cycling, there is a novel peak arising at a lower position of ~705.1 eV, which is assigned to a chemical condition of Fe^{2+} (Fe-S bond). Similarly, the Ni $2p_{3/2}$ XPS spectrum (Fig. 5f) of cycled cathodes also shows a new peak redshifted to ~853.2 eV, which can be elucidated by the formation of Ni-S bond. Given the absence of crystalline phase changes on $NiFe_2O_4$ QDs judged by previous XRD analysis, we conclude that strong chemical interactions between $NiFe_2O_4$ QDs and polysulfides should be the most convincing reason to account for above results [40–43].

4 Conclusions

In summary, low-cost and multi-functionalized $NiFe_2O_4$ QDs with exceptional electrolyte wettability, rich surface adsorption/catalytic sites, and good electrical conductivity have been used as additive substitutes to curtail the carbon usage and hence build more practical S cathodes for Li–S cells. The carbon content can be greatly decreased from ~26% (a mean percentage level in S/C hybrids) to a low value of ~5% for our S@CB⊆QDs. We also affirm $NiFe_2O_4$ QDs additives own excellent chemisorption interactions with soluble polysulfide molecules and prominent catalytic properties for Li_2S_n phase conversions and meantime boost the charge-transfer capability/redox kinetics of entire cathode systems. As a consequence, the designed S@CB⊆QDs hybrid cathodes demonstrate outstanding rate behaviors and quite stable cyclic performance in $LiNO_3$-free electrolytes (only ~0.08% capacity fade per cycle in 500 cycles at 0.2 A g^{-1}; Coulombic efficiency stays above 96%). Our present work may have great potential for the rational design of low-carbon-content electrodes and meanwhile arise tremendous research interest in exploiting more optional/useful QDs additives for practical Li–S cell systems.

Acknowledgments The authors sincerely thank financial supports from National Natural Science Foundation of China (51802269 and 21773138), Chongqing Natural Science Foundation (cstc2018jcyjAX0624), Fundamental Research Funds for the Central Universities (XDJK2019AA002), and Venture & Innovation Support Program for Chongqing overseas returnees (cx2018027).

Electronic supplementary material The online version of this article (https://doi.org/10.1007/s40820-020-00484-4) contains supplementary material, which is available to authorized users.

References

1. J. Cheng, J. Shang, Y.M. Sun, L.K. Ono, D.R. Wang et al., Flexible and stable high-energy lithium-sulfur full batteries with only 100% oversized lithium. Nat. Commun. **9**, 4480 (2018). https://doi.org/10.1038/s41467-018-06879-7
2. Z.L. Xu, S.H. Lin, N. Onofrio, L.M. Zhou, F.Y. Shi, W. Lu, K. Kang, Q. Zhang, S.P. Lau, Exceptional catalytic effects of black phosphorus quantum dots in shuttling-free lithium sulfur batteries. Nat. Commun. **9**, 4164 (2018). https://doi.org/10.1038/s41467-018-06629-9
3. L.L. Fan, M. Li, X.F. Li, W. Xiao, Z.W. Chen, J. Lu, Interlayer material selection for Lithium-Sulfur batteries. Joule **3**, 361–386 (2019). https://doi.org/10.1016/j.joule.2019.01.003
4. J. Pu, Z.H. Shen, J.X. Zheng, W.L. Wu, C. Zhu et al., Multifunctional Co_3S_4@sulfur nanotubes for enhanced Lithium-Sulfur battery performance. Nano Energy **37**, 7–14 (2017). https://doi.org/10.1016/j.nanoen.2017.05.009
5. Z.H. Li, Q. He, X. Xu, Y. Zhao, X.W. Liu et al., A 3D nitrogen-doped graphene/TiN nanowires composite as a strong polysulfides anchor for lithium-sulfur batteries with enhanced rate performance and high areal capacity. Adv. Energy Mater. **30**, 1804089 (2018). https://doi.org/10.1002/adma.201804089
6. S. Choi, C. Kim, J.M. Suh, H.W. Jang, Reduced graphene oxide-based materials for electrochemical energy conversion reactions. Carbon Energy **1**, 85–108 (2019). https://doi.org/10.1002/cey2.13
7. Y. Zhong, X.H. Xia, S.J. Deng, J.Y. Zhan, R.Y. Fang et al., Popcorn inspired porous macrocellular carbon: rapid puffng fabrication from rice and its applications in lithium-sulfur batteries. Adv. Energy Mater. **8**, 1701110 (2017). https://doi.org/10.1002/aenm.201701110
8. Y.Y. Shi, G.J. Liu, R.C. Jin, H. Xu, Q.Y. Wang, S.M. Gao, Carbon materials from melamine sponges for supercapacitors and lithium battery electrode materials: a review. Carbon Energy **1**, 253–275 (2019). https://doi.org/10.1002/cey2.19
9. F. Liu, C.J. Wang, X. Sui, M.A. Riaz, M.Y. Xu, L. Wei, Y. Chen, Synthesis of graphene materials by electrochemical exfoliation: recent progress and future potential. Carbon Energy **1**, 173–199 (2019). https://doi.org/10.1002/cey2.14
10. Q. Wu, L.J. Yang, X.Z. Wang, Z. Hu, From carbon-based nanotubes to nanocages for advanced energy conversion and storage. Acc. Chem. Res. **50**, 435–444 (2017). https://doi.org/10.1021/acs.accounts.6b00541
11. A. Bhargav, J.R. He, A. Gupta, A. Manthiram, Lithium-sulfur batteries: attaining the critical metrics. Joule **4**, 1–6 (2020). https://doi.org/10.1016/j.joule.2020.01.001
12. S.H. Chung, C.H. Chang, A. Manthiram, Progress on the critical parameters for lithium-sulfur batteries to be practically viable. Adv. Funct. Mater. **28**, 1801188 (2018). https://doi.org/10.1002/adfm.201801188
13. M.J. Klein, G.M. Veith, A. Manthiram, Rational design of lithium-sulfur battery cathodes based on experimentally determined maximum active material thickness. J. Am. Chem. Soc. **139**, 9229–9237 (2017). https://doi.org/10.1021/jacs.7b03380
14. J.J. Park, J.H. Moon, C.J. Kim, J.H. Kang, E. Lim et al., Graphene quantum dots: structural integrity and oxygen functional groups for high sulfur/sulfide utilization in lithium sulfur batteries. NPG Asia Mater. **8**, e272 (2016). https://doi.org/10.1038/am.2016.61
15. X.Y. Tao, J.G. Wang, Z.J. Ying, Q.X. Cai, G.Y. Zheng et al., Strong sulfur binding with conducting magnéli-phase $TinO_{2n-1}$ nanomaterials for improving lithium-sulfur batteries. Nano Lett. **14**, 5288–5294 (2014). https://doi.org/10.1021/nl502331f
16. X. Liang, C. Hart, Q. Pang, A. Garsuch, T. Weiss, L.F. Nazar, A highly efficient polysulfide mediator for lithium-sulfur batteries. Nat. Commun. **6**, 5682 (2015). https://doi.org/10.1038/ncomms6682
17. S.S. Zhang, D.T. Tran, Pyrite FeS_2 as an efficient adsorbent of lithium polysulphide for improved lithium-sulfur batteries. J. Mater. Chem. A **4**, 4371–4374 (2016). https://doi.org/10.1039/C6TA01214K
18. M. Nawwar, R. Poon, R. Chen, R.P. Sahu, I.K. Puri, I. Zhitomirsky, High areal capacitance of Fe_3O_4-decorated carbon nanotubes for supercapacitor electrodes. Carbon Energy **1**, 124–133 (2019). https://doi.org/10.1002/cey2.6
19. X. Liu, J.Q. Huang, Q. Zhang, L.Q. Mai, Nanostructured metal oxides and sulfdes for lithium-sulfur batteries. Adv. Mater. **29**, 1601759 (2017). https://doi.org/10.1002/adma.201601759
20. X. Liang, C.Y. Kwok, F. Lodi-Marzano, Q. Pang, M. Cuisinier et al., Tuning transition metal oxide-sulfur interactions for long life lithium sulfur batteries: the "Goldilocks" principle. Adv. Energy Mater. **6**, 1501636 (2016). https://doi.org/10.1002/aenm.201501636
21. Y. Lu, X.N. Li, J.W. Liang, H. Lei, Y.C. Zhu, Y.T. Qian, A simple melting-diffusing-reacting strategy tofabricate S/NiS_2-C for lithium-sulfur batteries. Nanoscale **8**, 17616–17622 (2016). https://doi.org/10.1039/c6nr05626a
22. Y. Li, J. Chen, Y.F. Zhang, Z.Y. Yu, T.Z. Zhang, W.Q. Ge, L.P. Zhang, NiS_2/rGO/S capable of lithium polysulfide trapping as an enhanced cathode material for lithium sulfur batteries. J. Alloy. Compd. **766**, 804–812 (2018). https://doi.org/10.1016/j.jallcom.2018.06.369
23. Q. Fan, W. Liu, Z. Weng, Y.M. Sun, H.L. Wang, Ternary hybrid material for high-performance lithium-sulfur battery. J. Am. Chem. Soc. **137**, 12946–12953 (2015). https://doi.org/10.1021/jacs.5b07071
24. X.T. Gao, Y. Xie, X.D. Zhu, K.N. Sun, X.M. Xie et al., Ultrathin MXene nanosheets decorated with TiO_2 quantum dots as an effcient sulfur host toward fast and stable Li-S batteries. Small **14**, 1802443 (2018). https://doi.org/10.1002/smll.201802443
25. Y. Hu, W. Chen, T.Y. Lei, B. Zhou, Y. Jiao et al., Carbon quantum dots-modified interfacial interactions and ion conductivity for enhanced high current density performance in Lithium-Sulfur batteries. Adv. Energy Mater. **9**, 1802955 (2018). https://doi.org/10.1002/aenm.201802955
26. R.P. Fang, S.Y. Zhao, S.F. Pei, X.T. Qian, P.X. Hou, H.M. Cheng, C. Liu, F. Li, Toward more eeliable lithium-sulfur batteries: an all-graphene cathode structure. ACS Nano **10**, 8682–8686 (2016). https://doi.org/10.1021/acsnano.6b04019

27. A.J. Ahlawat, V.G. Sathe, V.R. Reddy, A.M. Gupta, Raman and X-ray diffraction studies of superparamagnetic $NiFe_2O_4$ nanoparticles prepared by sol-gel auto-combustion method. J. Magn. Magn. Mater. **323**, 2049–2054 (2011). https://doi.org/10.1016/j.jmmm.2011.03.017
28. A.J. Ahlawat, V.G. Sathe, Raman study of $NiFe_2O_4$ nanoparticles, bulk and films: effect of laser power. J. Raman Spectrosc. **42**, 1087–1094 (2011). https://doi.org/10.1002/jrs.2791
29. S. Deng, Y. Zhong, Y. Zeng, Y. Wang, X. Wang et al., Hollow TiO_2@Co_9S_8 core-branch arrays as bifunctional electrocatalysts for efficient oxygen/hydrogen production. Adv. Sci. **5**, 1700772 (2018). https://doi.org/10.1002/advs.201700772
30. Y. Wang, R. Zhang, Y.C. Pang, X. Chen, J. Lang et al., Carbon@Titanium nitride dual shell nanospheres as multifunctional hosts for lithium sulfur batteries. Energy Storage Mater. **16**, 228–235 (2019). https://doi.org/10.1016/j.ensm.2018.05.019
31. L. Zhang, Z. Chen, F.N. Dong, M. Li, C. Diao et al., Nickel-cobalt double hydroxide as a multifunctional mediator for ultrahigh-rate and ultralong-life Li-S batteries. Adv. Energy Mater. **8**, 1802431 (2018). https://doi.org/10.1002/aenm.201802431
32. X.D. Jia, Y.F. Zhao, G.B. Chen, L. Shang, R. Shi et al., Water splitting: Ni_3FeN nanoparticles derived from ultrathin NiFe-layered double hydroxide nanosheets: an efficient overall water splitting electrocatalyst. Adv. Energy Mater. **6**, 1502585 (2016). https://doi.org/10.1002/aenm.201502585
33. J. Xu, W. Zhang, H. Fan, F. Cheng, D. Su, G. Wang, Promoting lithium polysulfides/sulfide redox kinetics by the catalyzing of zinc sulfide for high performance Lithium-Sulfur battery. Nano Energy **51**, 73–82 (2018). https://doi.org/10.1016/j.nanoen.2018.06.046
34. K. Xi, D. He, C. Harris, Y. Wang, C. Lai et al., Enhanced sulfur transformation by multifunctional FeS_2/FeS/S composites for high-volumetric capacity cathodes in Lithium-Sulfur batteries. Adv. Sci. **6**, 1800815 (2019). https://doi.org/10.1002/advs.201800815
35. L.Y. Hu, C.L Dai, H. Liu, Y. Li, B.L. Shen et al., Double-shelled NiO-$NiCo_2O_4$ heterostructure@carbon hollow nanocages as an effcient sulfur host for advanced lithium-sulfur batteries. Adv. Energy Mater. **8**, 1800709 (2018). https://doi.org/10.1002/aenm.201800709
36. Z.F. Deng, Z.A. Zhan, Y.Q. Lai, J. Liu, J. Li, Y.X. Liu, Electrochemical impedance spectroscopy study of a lithium/sulfur battery: modeling and analysis of capacity fading. J. Electrochem. Soc. **160**, A553–A558 (2013). https://doi.org/10.1149/2.026304jes
37. W.W. Zeng, L. Wang, X. Peng, T.F. Liu, Y.Y. Jiang et al., Enhanced ion conductivity in conducting polymer binder for high-performance silicon anodes in advanced lithium-ion batteries. Adv. Energy Mater. **8**, 1702314 (2018). https://doi.org/10.1002/aenm.201702314
38. H.J. Peng, Z.W. Zhang, J.Q. Huang, G. Xie, J. Zhang et al., A cooperative interface for highly efficient lithium-sulfur batteries. Adv. Mater. **28**, 9551–9558 (2016). https://doi.org/10.1002/adma.201603401
39. M. Zhao, H.J. Peng, Z.W. Zhang, B.Q. Li, X. Chen et al., Activating inert metallic compounds for high-rate lithium-sulfur batteries through in situ etching of extrinsic metal. Angew. Chem. Int. Ed. **58**, 3779–3783 (2019). https://doi.org/10.1002/anie.201812062
40. G.E. LeCroy, S.K. Sonkar, F. Yang, L.M. Veca, P. Wang et al., Toward structurally defined carbon dots as ultracompact fluorescent probes. ACS Nano **8**, 4522–4529 (2014). https://doi.org/10.1021/nn406628s
41. Y. Hu, M.M. Awak, F. Yang, S.J. Yan, Q.W. Xiong et al., Photoexcited state properties of carbon dots from thermally induced functionalization of carbon nanoparticles. J. Mater. Chem. C **4**, 10554–10561 (2016). https://doi.org/10.1021/nn406628s
42. W.L. Wu, J. Pu, J. Wang, Z.H. Shen, H.Y. Tang et al., Biomimetic bipolar microcapsules derived from staphylococcus aureus for enhanced properties of lithium-sulfur battery cathodes. Adv. Energy Mater. **8**, 1702373 (2018). https://doi.org/10.1002/aenm.201702373
43. T. Liu, C.J. Jiang, B. Cheng, W. You, J.G. Yu, Hierarchical NiS/N-doped carbon composite hollow spheres with excellent supercapacitor performance. J. Mater. Chem. A **5**, 21257–21265 (2017). https://doi.org/10.1039/C7TA06149H

 https://doi.org/10.1007/s40820-020-00484-4